ACS APPLIED MATERIALS & INTERFACES

Energy, Environmental, and Catalysis Applications

Three MOFs-Templated Carbon Nanocompoites for Potential Platforms of Enzyme Immobilization with Improved Electrochemical Performance

Sheying Dong, Lei Peng, Wenbo Wei, and Tinglin Huang

ACS Appl. Mater. Interfaces, **Just Accepted Manuscript** • DOI: 10.1021/acsami.8b00702 • Publication Date (Web): 05 Apr 2018

Just Accepted

ACS Publications

is published by the American Chemical Society. 1155 Sixteenth Street N.W., Washington, DC 20036

Three MOF-templated Carbon Nanocomposites for Potential Platforms of Enzyme Immobilization with Improved Electrochemical Performance

Sheying Dong[*†§], *Lei Peng*[‡§], *Wenbo Wei*[†], *and Tinglin Huang*[§]

[†] College of Sciences, Xi′an University of Architecture and Technology, Xi′an 710055, People's Republic of China

[‡] Institute of Environmental and Food Safety, Wuhan Academy of Agricultural Science and Technology, Wuhan, 430207, People's Republic of China

[§] School of Environmental and Municipal Engineering, Xi′an University of Architecture and Technology, Xi′an 710055, People's Republic of China

*Corresponding author. Phone: (+86)-29-82201203. Fax: (+86)-29-82205332.

E-mail address: dongsyy@126.com (S.Y. Dong)

*Corresponding author. Tel.: +86 29 82201203; fax: +86 29 82205332.

E-mail address: dongsyy@126.com

ABSTRACT. An efficient and facile MOF-template strategy for preparing carbon nanocomposites has been developed. First of all, a series of metal ions including Fe^{3+}, Zr^{4+} and La^{3+} were respectively connected with 2-aminoterephthalate (H_2ATA) to form three metal–organic frameworks (MOFs), and then three novel MOF-derived materials were obtained by annealing them at 550 °C under N_2 atmosphere. The morphologies and microstructures results showed that they still retained the original structure of MOFs, and formed carbon supported-metal oxide hybrid nanomaterials. Interestingly, it was found that La-MOF-NH_2 and its derived materials were firstly reported, which had wool-ball-like structure formed by many streaky-shaped intertwining each other. Furthermore, these MOF-derived materials were all successfully used as effective immobilization matrixes of acetylcholinesterase (AChE) to construct biosensors for the detection of methyl parathion. Especially, [La-MOF-NH_2]$_{N2}$ structure with wool-ball-like not only provided more active sites of mulit-contents to increase AChE immobilization amount, but also facilitated the accessibility of electron transfer and shorten their diffusion length on the surface of electrode. Under optimal conditions, the biosensor based on [La-MOF-NH_2]$_{N2}$ displayed the widest linear range of 1.0×10^{-13}-5.0×10^{-9} g·mL^{-1} and the lowest detection limit of 5.8×10^{-14} g·mL^{-1} in three biosensors. This study illustrates the feasibility and the potential of a series of MOF-derived materials for biosensors with improved electrochemical performance.

KEYWORDS: MOF-derived materials; Carbon-based nanocomposites; AChE immobilization; Organophosphate pesticide; Electrochemical biosensor

INTRODUCTION. MOFs have drawn considerable attention in the latest decades due to their tunable structures, versatile functionalities and multiple applications. [1-6] Since Liu et al. reported firstly the MOF-5 framework as a template for preparing nanoporous carbon materials, a lot of research work has been focused on the preparation of various nanomaterials derived from MOFs precursors. [7-10] Among MOF-derived materials, the carbon supported-metal oxide hybrid nanomaterials with large pore volume and superior conductivity enable a high degree of homogenous dispersion of metal oxide species within carbon matrix, preventing the metal oxide from self-accumulation. This is extremely beneficial to the electrochemical performance of electrode materials. For example, Zhang and co-workers synthesized porous Co_3O_4/C nanowire arrays by thermally annealing Co-MOF. The hybrid material manifested not only a high specific capacitance (1.32 F cm^{-2} at 1 mA cm^{-2}) but also an outstanding electrochemical catalysis ability for oxygen evolution reaction (OER). [11] Zheng et al. reported an ultrafine MnO nanocrystals encapsulated in porous carbon matrix (MnO@C) derived from Mn-based MOF, and these MnO@C composites displayed a high reversible specific capacity of 1221 mAh g^{-1} after 100 cycles at a current density of 100 mA g^{-1} when evaluated as an anode material for lithium-ion batteries (LIBs). [12]

Most of studies of MOF-derived materials mainly focus on the synthesis and their application in electrode materials such as supercapacitor, fuel cells and batteries. Nevertheless, there has been few researches on the enzyme immobilization matrix for electrochemical biosensor through direct thermal decomposition of MOFs. For such

analytical application, highly electroconductive nanomaterials with improved capability for the stable immobilization of enzymes are mainly desired.

The construction of MOFs is mainly based on the diversity of metal oxide clusters which can be connected with innumerous functionalized organic linkers. As a linear organic linker, 1,4-benzenedicarboxylate has been widely used because it leads to the formation of many open-framework structures with interesting features. [13]Especially, the linker can combine with trivalent metal cations, such as Al^{3+}, Fe^{3+} and Cr^{3+} under solvothermal synthetic conditions to form MOFs. [14-16] Zr^{4+} cation was also used in the field of self-assembly to connect 12 dicarboxylate linkers to form MOFs. Just lately, the amino-functionalized MOF form of MIL-53 has been described. [17] However, up to the present knowledge, another trivalent metal cations (La^{3+}), synthesis of La-MOF by the combination with H_2BDC or amino-functionalized H_2BDC has not been reported. More importantly, these metals-based oxides and their composites have good electrocatalytic property and biocompatibility, which are benefit for enzyme electrochemical biosensor.

Electrochemical biosensors remain attractive for their on-site analysis, fast response, high sensitivity and relatively cheap instrumentation. [18-20] As far as known, a key issue in terms of enzyme immobilization has been limiting their performance for electrochemical biosensors. To seek for better immobilization matrixes, various materials have been effectively used as the immobilization of enzymes for enhancing electrochemical performances. [21,22] However, these strategies are also subjected to the shortcomings of low loading capacity and leakage of enzymes molecules. Therefore,

developing a new matrix with good biocompatibility, enhancing conductivity and catalytic property for the immobilization of enzymes is very important. More recently, MOFs have been used as electrochemical platforms to improve the sensitivity and limits of detection. [23-25] The introduction of MOF-derived materials into enzymatic biosensors for the detection of pesticides is still unexplored and lack of relevant literatures. With further exploiting application of MOFs, MOF-derived materials could be a more attractive and favorable alternative in the construction of biosensors because of their better electrical conductivity and mechanical stability.

In this work, three MOFs such as Fe-MOF-NH_2, Zr-MOF-NH_2 and La-MOF-NH_2 were prepared by solvothermal method. After further carbonization under an N_2 atmosphere, these MOFs were converted to corresponding carbon nanocomposites, which were homogeneously dispersed in nafion (NF) solution respectively as matrix immobilizing AChE for the detection of methyl parathion. As a result, the biosensor based on $[La\text{-}MOF\text{-}NH_2]_{N2}$ with special structure has best electrochemical performance. As far as we known, it's the first example of making use of MOF with wool-ball-like structure as a precursor to prepare novel carbon-based composites and to construct electrochemical biosensor.

EXPERIMENTAL SECTION

The **chemicals**, **apparatus** and **electrochemical measurements** were described in the **Supporting Information**.

Synthesis of MOFs. M-MOF-NH_2 (M: Fe, Zr, La) was prepared as described previously with some modifications [26] in the **Supporting Information**.

Synthesis of Carbon Nanocomposites. Under N_2 flow, the as-obtained Fe-MOF-NH_2 was carbonized at 550 °C for 2 h. The product of black powder was expressed as the [Fe-MOF-NH_2]$_{N2}$. Zr-MOF-NH_2 and La-MOF-NH_2 were further calcined at the same conditions, denoted as [Zr-MOF-NH_2]$_{N2}$, and [La-MOF-NH_2]$_{N2}$, respectively.

Biosensor Fabrication. CPE was fabricated according to our previous report, [27] and the detail was described in the **Supporting Information**.

The preparation of AChE biosensor: Firstly, 3 mg of [M-MOF-NH_2]$_{N2}$ powders were dispersed into 1mL 0.1 M pH 7.0 PBS containing 0.1% (Wt/V) NF under sonication for 30 min to obtain homogeneous NF-[M-MOF-NH_2]$_{N2}$ suspension. Following that 6 μL of suspension above was coated onto a freshly polished CPE surface to get NF-[M-MOF-NH_2]$_{N2}$/CPE, which was naturally dried at room temperature for a stable film. Furthermore, AChE/NF-[M-MOF-NH_2]$_{N2}$/CPE was obtained by dropping 7 μL of 0.2 mg·mL^{-1} AChE solution onto NF-[M-MOF-NH_2]$_{N2}$/CPE and then was placed in a refrigerator at 4 °C as well as washed with doubly distilled water for two or three times for removing the free AChE molecules. Finally, the AChE/NF-[M-MOF-NH_2]$_{N2}$/CPE was covered with 5 μL of 0.5 % (Wt/V) NF as the protective layer to get NF/AChE/NF-[M-MOF-NH_2]$_{N2}$/CPE and placed in 0.1 M pH 7.0 PBS in a refrigerator at 4 °C.

Methyl Parathion Detection. The NF/AChE/NF-[M-MOF-NH_2]$_{N2}$/CPE was used for the analysis of methyl parathion by DPV approach. The biosensor performance was evaluated via its DPV response in 0.1M pH 7.0 PBS solution with

0.5 mM ATCl. The biosensor was washed with doubly distilled water, and then incubated in the certain concentration of methyl parathion for 12 min. In the end, the biosensor was transferred into the 0.1M pH 7.0 PBS solution with 0.5 mM ATCl to perform DPV experiment under the same conditions. The inhibition rate of methyl parathion was estimated as below (Eq.1): [21]

$$\text{Inhibition (\%)} = (i_{p,control} - i_{p,exp})/i_{p,control} \times 1\ 00\% \quad (1)$$

Where I_0 and I_i are the peak current of 0.5 mM ATCl before and after exposure with different concentrations of methyl parathion. There is a linear relationship between the inhibition (%) and the logarithm of concentrations of the methyl parathion.

RESULTS AND DICUSSION

Synthesis and Characterizations of Three Carbon Nanocomposites.

The synthesis route of carbon nanocomposites was shown in **Scheme. 1**. First, Fe^{3+}, Zr^{4+} and La^{3+} as metal center units, and H_2ATA as organic linkers, three MOFs were synthesized under the solvothermal reaction, which exhibited brown, light yellow and orange, respectively (**Figure 1a**). Second, these MOFs were further calcined to obtain carbon nanocomposites.

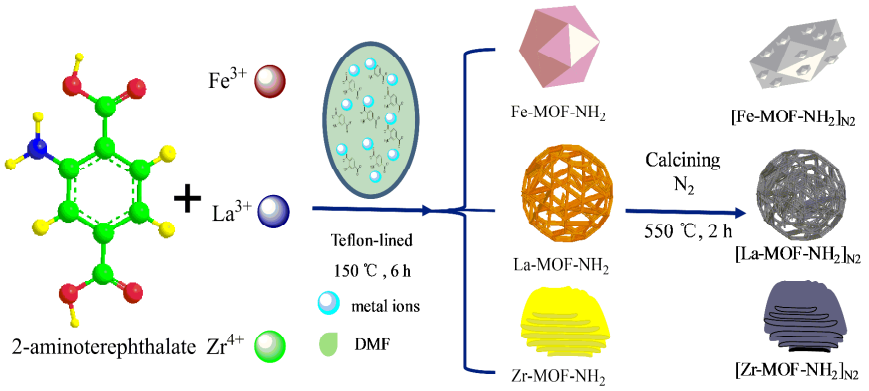

Scheme 1. Schematic Illustration of the fabrication processes of $[M\text{-}MOF\text{-}NH_2]_{N2}$

Scanning electron microscopy (SEM) images given in **Figure 1b** and **Figure 1c** clearly show the flat spindle structure with a uniform particles and size for the Fe-MOF-NH_2 and wafer accumulation structure for Zr-MOF-NH_2. Interestingly, as shown in SEM image in **Figure 1d**, La-MOF-NH_2 was wool-ball-like which was formed by many streaky-shaped intertwining each other. Enlarged view of SEM image in its inset showed that these streaky-shaped were assembled from many scales structures of relatively uniform. Furthermore, the structure of the M-MOF-NH_2 nanocomposites were revealed by transmission electron microscopy (TEM). The uniform flat spindle structure for the Fe-MOF-NH_2 (**Figure 1e**) and wafer accumulation structure for Zr-MOF-NH_2 (**Figure 1f**) were seen clearly. As shown in **Figure 1g,** many intertwined tiny-needles can be observed on the La-MOF-NH_2 rough surface.

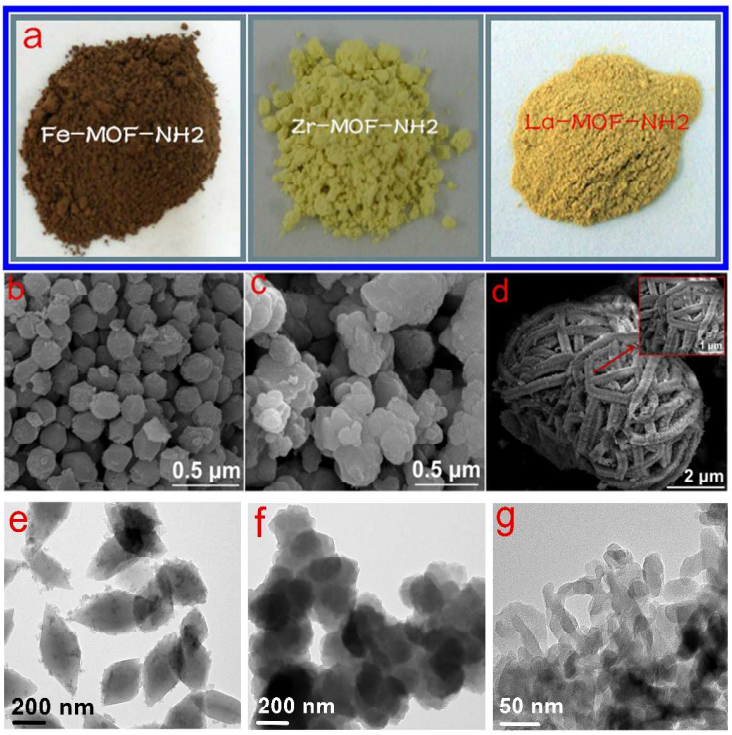

Figure 1. (a)The digital photos Fe-MOF-NH_2 , Zr-MOF-NH_2, La-MOF-NH_2 ; (b, c, d) SEM and (e, f, g) TEM images of Fe-MOF-NH_2 , Zr-MOF-NH_2 and La-MOF-NH_2, respectively.

As clearly seen in the powder XRD of **Figure S1**, the diffraction patterns of the as-prepared Fe-MOF-NH_2 are consistent with result of the previous reports. [26] Here Zr-MOF-NH_2 has similar diffraction peaks to the Zr-MOFs prepared by other condition, [28] but the peaks were weak. La-MOF-NH_2 have obvious diffraction peaks, demonstrating that lanthanum ions have been successfully coordinated with H_2BDC ligands to form MOF.

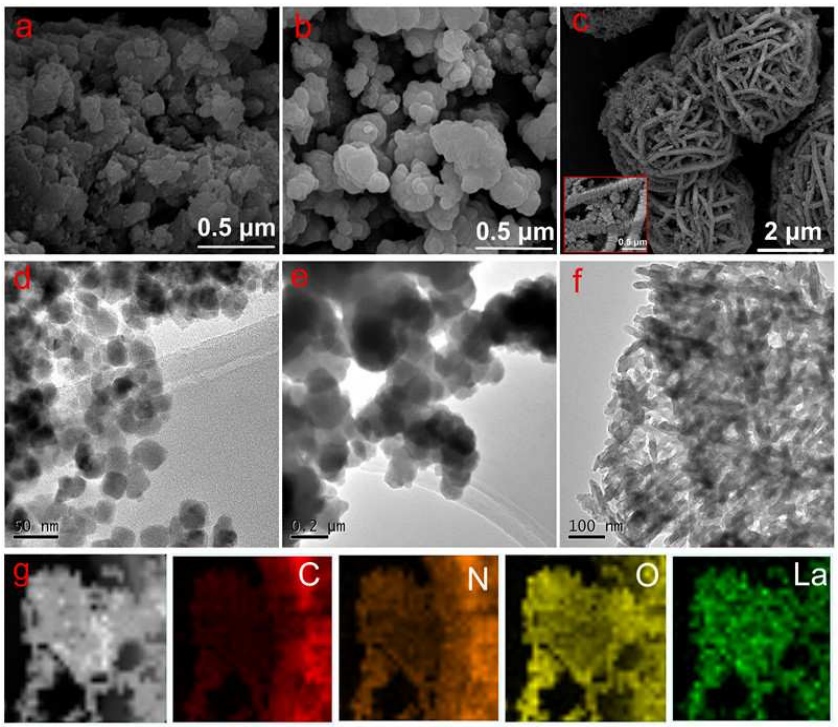

Figure 2. The SEM and TEM image of (a,d) $[Fe\text{-}MOF\text{-}NH_2]_{N2}$ (b,e) $[Zr\text{-}MOF\text{-}NH_2]_{N2}$ (c,f)$[La\text{-}MOF\text{-}NH_2]_{N2.}$ (g) Elemental mapping showing the uniform dispersion of C, N, O, and La elements.

Carbon nanocomposites were synthesized through thermal treatment of three MOFs at 550 °C under N_2 atmosphere. **Figure 2a-c** show the SEM images of these products including $[Fe\text{-}MOF\text{-}NH_2]_{N2}$, $[Zr\text{-}MOF\text{-}NH_2]_{N2}$ and $[La\text{-}MOF\text{-}NH_2]_{N2}$. After the thermal treatment, their original morphologies are still retained. In particular, the $[La\text{-}MOF\text{-}NH_2]_{N2}$ not only remains wool-ball-like morphology along with a well-preserved macroscopic structure，but also loose structures appear in the streaky-shaped intertwining each other，which are more conducive to the subsequent immobilization of enzymes. This phenomenon is perhaps due to the emission gas in the calcination process of $La\text{-}MOF\text{-}NH_2$. In the synthesis process, the mixing of $La(NO_3)_3{\cdot}6H_2O$ and H_2ATA with DMF solution formed the nucleation which would

crystallize and self-assemble to form streaky-shaped particles under solvothermal conditions. With solvothermal treatment time prolonging, these streaky-shaped particles would intertwine with each other to form wool-ball-like particles. Element analysis from SEM-EDS (**Figure S2**) method verifies the presence of C, O and corresponding metal elements in these MOF-derived materials.

The structures of as-derived materials were further examined by TEM as depicted in **Figure 2d-f**. The uniform particles were composed of numerous small nanocrystallites that were uniformly dispersed in the carbon matrix. The elemental mapping as shown in **Figure 2g** confirmed the homogeneous distribution of C, N, O and La elements in the MOF-derived materials.

Figure 3A depicted the XRD patterns of the as-synthesized $[Fe\text{-}MOF\text{-}NH_2]_{N2}$, $[Zr\text{-}MOF\text{-}NH_2]_{N2}$ and $[La\text{-}MOF\text{-}NH_2]_{N2}$ samples. Compared with those of MOFs, their diffraction peaks are obviously different. It can be observed that all the samples exhibited a broad diffraction peaks around 24.0^o, corresponding to diffraction from the (002) crystalline planes of graphite carbon. $[Fe\text{-}MOF\text{-}NH_2]_{N2}$ shows obvious Fe_2O_3 peaks，[29] indicating the formation of Fe_2O_3 in $[Fe\text{-}MOF\text{-}NH_2]_{N2}$. The peaks of $[Zr\text{-}MOF\text{-}NH_2]_{N2}$ at 30.18°, 50.2°, and 59.98° correspond to the respective (111), (202) and (131) planes of square ZrO_2, respectively. No peaks belonging to metallic La and its oxide phase are detected because of its low content.

Raman spectra of the three samples were also performed to further compare their graphitic structure, as shown in **Figure 3B**. Typical G and D bands located at 1587 cm^{-1} and 1348 cm^{-1} represented that the hexagonally bonded carbon atoms inside the

graphitic networks and the distorted carbon frames on the defect sites.[30] The ratio of integrated intensities of the D band to the G band (I_D/I_G) was calculated to be 0.861 ($[La\text{-}MOF\text{-}NH_2]_{N2}$), lower than that of 0.896 ($[Fe\text{-}MOF\text{-}NH_2]_{N2}$) and 1.07 ($[Zr\text{-}MOF\text{-}NH_2]_{N2}$), showing the higher graphitic degree of $[La\text{-}MOF\text{-}NH_2]_{N2}$, which was benefit for improving the electric conductivity .

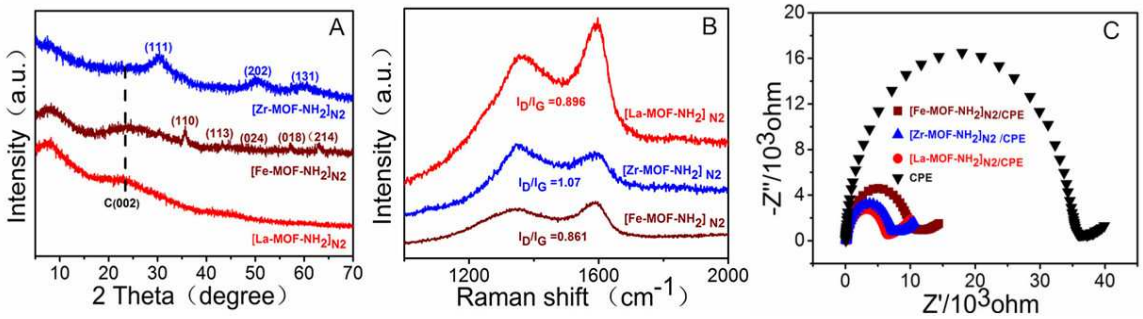

Figure 3. The XRD patterns (A) and Raman spectra (B) of $[Fe\text{-}MOF\text{-}NH_2]_{N2}$, $[Zr\text{-}MOF\text{-}NH_2]_{N2}$ and $[La\text{-}MOF\text{-}NH_2]_{N2}$ (C) Electrochemical impedance spectra of CPE, $[Fe\text{-}MOF\text{-}NH_2]_{N2}$/CPE, $[Zr\text{-}MOF\text{-}NH_2]_{N2}$/CPE and $[La\text{-}MOF\text{-}NH_2]_{N2}$/CPE in the solution of 5.0 mM $K_3Fe(CN)_6/K_4Fe(CN)_6$ (1:1) containing 0.1 M KCl. Amplitude: 0.005 V; the frequencies: 10^5 to 10^{-2} Hz; bias potential: 0.20 V.

In addition, the effect of the modification process on the impedance of the electrode surface was investigate by electrochemical impedance spectroscopy (EIS). **Figure 3C** displayed the representative impedance spectra of the bare CPE and these carbon supported-metal oxide hybrid nanomaterials modified CPE in 5.0 mM $K_3Fe(CN)_6/K_4Fe(CN)_6$ (1:1) containing 0.1 M KCl. In the high frequency section, the high electron transfer resistance (R_{ct}) of the bare CPE indicated an inefficient electron transfer process on the surface of CPE.[31] After the bare CPE was modified with

MOF-derived material, their R_{ct} values declined obviously and were in the order of their R_{ct} values were in the trend of [Fe-MOF-NH_2]$_{N2}$/CPE＞[Zr-MOF-NH_2]$_{N2}$/CPE ＞[La-MOF-NH_2]$_{N2}$/CPE, suggesting high electric conductivity of these materials.

We performed a series of UV-Vis spectra experiments by Ellman's method [32] to attempt to clarify the interaction between AChE and the MOF-derived material. The UV-Vis spectra of (a) AChE (b) AChE/ [La-MOF-NH_2]$_{N2}$, (c) blank solutions were shown **in Figure S3**. The blank solution absorption band at 325 nm was attributed to 5, 5'-Dithiobis-(2-nitrobenzoic acid) (DTNB). Moreover, the absorption peak at about 411 nm in AChE and AChE/MOF-derived material solutions are approximately the same under the same condition. This was due to the reaction product of thiocholine with DNTB, indicating that there was only weak interaction, no strong interaction between AChE and the MOF-derived materials. As a result, these MOF-derived materials with suitable microenviroment have good biocompatibility for AChE immobilization.

Optimization of Experiment Parameters. Various experiment parameters, such as pH values of PBS, AChE amount, volume of NF-[La-MOF-NH_2]$_{N2}$ and incubation time, were separately investigated for better performance of biosensor in the **Figure S4A-D** and the detail was described in the **Supporting Information**. As result, a pH 7.0 of PBS, 0.189 U of AChE, 6 μL of NF-[La-MOF-NH_2]$_{N2}$ and 12 min incubation time were chosen as the optimal parameters in the subsequent experiment.

Characterization of the Biosensor. As shown in **Figure 4A**, the CVs of

various electrodes were investigated in 0.1 M pH 7.0 PBS. As shown in the inset, there were no any peaks at (a′) NF/AChE/CPE, (b′) NF/AChE/NF-[Fe-MOF-NH_2]$_{N2}$/CPE, (c′) NF/AChE/NF-[Zr-MOF-NH_2]$_{N2}$/CPE and (d′) NF/AChE/NF-[La-MOF-NH_2]$_{N2}$/CPE for the lack of electroactive species in the examined range. Addition of 0.5 mM ATCl into the PBS, oxidation peak was still not observed at (a) NF/AChE/CPE. In contrast, oxidation peaks appeared on modified electrodes after the addition of 0.5 mM ATCl， and peak current increased in different degrees as following order: NF/AChE/NF-[La-MOF-NH_2]$_{N2}$/CPE > NF/AChE/NF-[Zr-MOF-NH_2]$_{N2}$/CPE > NF/AChE/NF-[Fe-MOF-NH_2]$_{N2}$/CPE. These irreversible oxidation peaks came from the oxidation of thiocholine (TCh). In detail, the immobilized AChE catalyzed the hydrolysis of ATCl to product electroactive TCh and acetic acid, and then the resultant TCh could be further oxidized on the surface of the electrode. [33]

The influence of the scan rate on the CV performance of three AChE electrodes were investigated in the presence of 0.5 mM ATCl. As shown in **Figure S5**, the intensity of anodic peaks increased continuously with increased scan rate from 0.04 to 0.3 V s^{-1}, and the peak currents (i_p) for ATCl were proportional to scan rate (v) (**Figure 4B**; linear regression equations: NF/AChE/NF-[Fe-MOF-NH_2]$_{N2}$/CPE：$i_{p,a}$(μA)= -13.05v(V s^{-1}) - 1.741(R=0.9987)；NF/AChE/NF-[Zr-MOF-NH_2]$_{N2}$/CPE：$i_{p,a}$(μA)= -13.27v(V s^{-1}) - 2.969(R=0.9976)；NF/AChE/NF-[La-MOF-NH_2]$_{N2}$/CPE：$i_{p,a}$(μA)= -22.24 (V s^{-1}) - 2.943(R=0.9932), indicating a surface-controlled process. [34]

Figure 4C showed typical current–time plots of NF/AChE/NF-[La-MOF-NH_2]$_{N2}$

/CPE, NF/AChE/NF-[Zr-MOF-NH_2]$_{N2}$/CPE and NF/AChE/NF-[Fe-MOF-NH_2]$_{N2}$/CPE under the optimum experimental conditions. With addition of ATCl to the buffer, the current increased and achieved 95 % of its steady state within 10 s. The response current increased linearly with the increasing ATCl concentration in the ranges of 0.5-502 μM for NF/AChE/NF-[Fe-MOF-NH_2]$_{N2}$/CPE, 0.4-612 μM for NF/AChE/NF-[Zr-MOF-NH_2]$_{N2}$/CPE and 0.2-705 μM for NF/AChE/NF-[La-MOF-NH_2]$_{N2}$/CPE. The detection limit of 0.3 μM, 0.16 μM, 0.1 μM was obtained at a signal to noise of 3 respectively. When the concentration of ATCl was very high, a platform was observed, showing a characteristic of the Michaelis-Menten kinetic mechanism. The Michaelis-Menten constant (K_M) value for the enzymatic activity of the NF/AChE/NF-[La-MOF-NH_2]$_{N2}$/CPE to ATCl was estimated with the Lineweaver–Burk equation (Eq.2): [35]

$$1/I_{ss} = 1/I_{max} + K_M /I_{max} \cdot 1/c \quad (2)$$

The K_M value was calculated via the slope and intercept for the plot of the reciprocals of the steady-state currents (I_{ss}) against ATCl concentrations. The K_m value was 0.575 mM, 0.413 mM and 0.167 mM respectively, which were much smaller than 0.18 mM of AChE/CMC/GCE, [36] indicating a higher affinity of the NF/AChE/NF-[La-MOF-NH_2]$_{N2}$/CPE to ATCl.

Possible Mechanism of Three Materials on Electrochemistry Performance. Compared with MOFs, these carbon nanocomposites derived from MOF materials are more suitable for enzyme immobilization support because of their better electrical conductivity and stability of electrodes. The enhanced

electrochemical response can be ascribed to the good conductivity of these MOF-derived materials. Meantime, MOFs-derived materials with more active sites of mulit-contents could be devoted to the increase of the electrocatalysis toward TCh. In addition, NF protective membrane was used to prevent the loss of AChE molecules, provide a biocompatible microenvironment to the maximum exposure of active sites of the AChE. Therefore, MOFs-derived materials in NF effectively promote the electrocatalysis toward TCh. In particular, it is notable that NF/AChE/NF-$[La\text{-}MOF\text{-}NH_2]_{N2}$/CPE has the best performance in all of them, which is mainly due to $[La\text{-}MOF\text{-}NH_2]_{N2}$ with superior structure. This wool-ball-like structure consists of more streaky-shaped intertwining and space each other, and many tiny needles can be observed on its rough surface. The wool-ball-like structure has the advantages that not only provides more active sites of mulit-contents and more suitable orientation to increase the immobilization amount of AChE, but also facilitates the accessibility of electron transfer for its higher electrical conductivity.

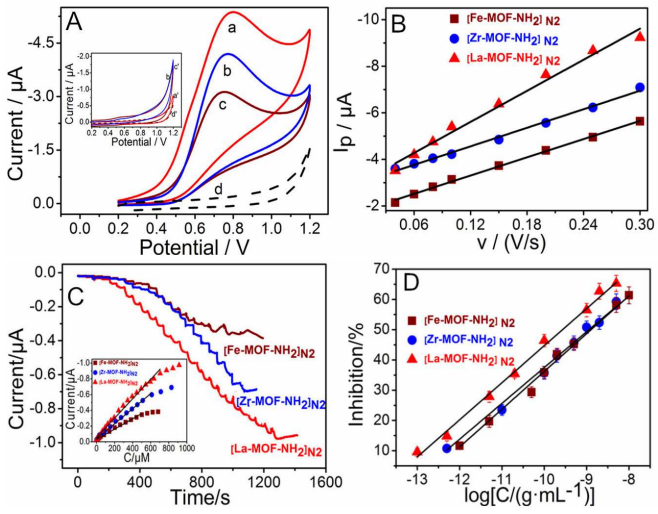

Figure 4. (A) CVs of (a/a′) NF/AChE/NF-[Fe-MOF-NH_2]$_{N2}$/CPE (b/b′) NF/AChE/NF-[Zr-MOF-NH_2]$_{N2}$/CPE (c/c′) NF/AChE/NF-[La-MOF-NH_2]$_{N2}$/CPE (d/d′) NF/AChE/CPE within/without 0.5 mM ATCl in 0.1 M pH 7.0 PBS (B) The plots of i_p vs. v (C) Amperometric current-time response curves of NF/AChE/NF-[Fe-MOF-NH_2]$_{N2}$/CPE, NF/AChE/NF-[Zr-MOF-NH_2]$_{N2}$/CPE and NF/AChE/NF-[La-MOF-NH_2]$_{N2}$/CPE upon successive addition of ATCl into 0.1 M pH 7.0 PBS solution. Applied potential: 0.76 V. Inset: calibration curves of steady-state currents vs. ATCl concentration at three AChE-based modified electrodes (D) their inhibition curves for methyl parathion.

Electrochemical Determination of Methyl Parathion. DPV measures were performed before and after incubation methyl parathion for 12 min in 0.1M pH 7.0 PBS with 0.5 mM ATCl **(Figure S6)**. As shown in the **Figure 4D**, the linear range were found to be 1.0×10^{-12}-1.0×10^{-8} g·mL^{-1} with the detection limit of 3.2×10^{-13} g·mL^{-1} for NF/AChE/NF-[Fe-MOF-NH_2]$_{N2}$/CPE, 5.0×10^{-13}-5.0×10^{-9} g·mL^{-1} with the detection limit of 1.8×10^{-13} g·mL^{-1} for NF/AChE/NF-[Zr-MOF-NH_2]$_{N2}$/CPE, and 1.0×10^{-13}-5.0×10^{-9} g·mL^{-1} with the detection limit of 5.8×10^{-14} g·mL^{-1} for

NF/AChE/NF-[La-MOF-NH_2]$_{N2}$/CPE respectively. Comparative studies with other AChE biosensors reported were summarized in Table 1. The results indicated that NF/AChE/NF-[La-MOF-NH_2]$_{N2}$/CPE had a wider range, and lower detection limit. Therefore, NF/AChE/NF -[La-MOF-NH_2]$_{N2}$/CPE biosensor would be an excellent platform for the detection of methyl parathion.

Table 1 Comparisons of the Performance of Different AChE Biosensors

Biosensors	Linear range	Detection limit	References
AChE/CNT–NH_2/GCE	0.2-1.0 and 1.0-30 nM	0.8×10^{-10} M	37
AChE/ CS@TiO_2-CS/rGO/GCE	0.036- 22.6 μM	2.9×10^{-5} M	38
AChE/HCS@PANI/GCE	10^{-9}-10^{-5} g·mL^{-1}	6.3×10^{-10} M	39
PLaE-CS/AuNPs-GNs/GCE	0.19 -760 nM	1.6×10^{-10} M	40
AChE/Silica sol-gel flim/CPE	0.1-0.5 ppb	3.3×10^{-10} M	41
AChE/AuNPs-CSs /BOD	10^{-12}-10^{-6} M	4.9×10^{-13} M	42
NF/AChE/ NF-$NiCo_2S_4$/CPE	10^{-12}-10^{-8}g·mL^{-1}	1.6×10^{-12} M	43
NF/AChE/NF-[Fe-MOF-NH_2]$_{N2}$/CPE	10^{-12}-10^{-8}g·mL^{-1}	3.2×10^{-13} g·mL^{-1} (1.2×10^{-12} M)	This work
NF/AChE/NF-[Zr-MOF-NH_2]$_{N2}$/CPE	5.0×10^{-13}-5.0×10^{-9}g·mL^{-1}	1.8×10^{-13} g·mL^{-1} (6.9×10^{-13} M)	This work
NF/AChE/NF-[La-MOF-NH_2]$_{N2}$/CPE	10^{-13}-5.0×10^{-9}g·mL^{-1}	5.8×10^{-14} g·mL^{-1} (2.2×10^{-13} M)	This work

The fabrication reproducibility for six NF/AChE/NF-[Fe-MOF-NH_2]$_{N2}$/CPE, NF/AChE/NF-[Zr-MOF-NH_2]$_{N2}$/CPE and NF/AChE/NF-[La-MOF-NH_2]$_{N2}$/CPE was performed by comparison of their currents in 0.1 M pH 7.0 PBS containing 0.5 mM ATCl. The relative standard deviation (RSD) was 4.8 %, 4.7 % and 4.5 % (n = 6), revealing an excellent reproducibility of the electrode preparation procedure. In addition, the electrode respectively retained 91 %，92 % and 92 % of its initial peak current after it was kept in refrigerator at 4 °C in pH 7.0 PBS for two weeks, and still retained 81 %，83 % and 84 % response under the same conditions after four weeks. The results show long-term stability of these AChE biosensors based on

carbon supported-metal oxide hybrid nanomaterials modified CPE.

CONCLUSIONS

Three MOFs were prepared by solvothermal synthetic conditions, and an effective and facile approach was developed to obtain corresponding MOF-derived materials that were novel carbon nanocomposites. Compared with MOFs, they were more suitable to be used as electrochemical sensing materials. Thereinto, $[La\text{-}MOF\text{-}NH_2]_{N2}$ has the best electrochemical performance, which might be mainly attributed to the multi-contents of the active species and robust structure of wool-ball-like structure formed by many streaky-shaped intertwining each other. Moreover, these electrochemical biosensors fabricated by immobilizing AChE exhibited high performance towards sensitive detection of methyl parathion under the optimum experimental conditions. This MOF precursor strategy can be extended in the design and synthesis of many other hybrid functional materials. Meantime, it also offers an effective method preparing highly active MOF-derived electrode materials for different enzymes immobilization in electrochemical biosensor applications.

ASSOCIATED CONTENT

The **Supporting Information** including additional experimental section, SEM-EDS, XRD and electrochemical results is available free of charge on http://pubs.acs.org

AUTHOR INFORMATION

Corresponding Author

*E-mail address: dongsyy@126.com (S.Y. Dong). Phone: (+86)-29-82201203. Fax: (+86)-29-82205332.

Notes

The authors declare no competing financial interest.

ACKNOWLEDGMENT

The authors appreciate the support from the National Natural Science Foundation of China (No. 21575111), Natural Science Foundation of Shaanxi Province (2017JM2038).

REFERENCES

(1) Yaghi, O. M.; Li, H. Synthesis of a metal-organic framework containing large rectangular channels, *J. Am. Chem. Soc*. **1995**, *117*, 10401-10402.

(2) Furukawa, H.; Ko, N.; Go, Y. B.; Aratani, N.; Choi, S. B.; Choi, E.; Yazaydin, A. O.; Snurr, R. Q.; O'Keeffe, M.; Kim, J.; Yaghi, O. M. Ultrahigh porosity in metal-organic frameworks. *Science* **2010**, *329*, 424-428.

(3) Furukawa, H.; Cordova, K. E.; O'Keeffe, M.; Yaghi, O. M. The chemistry and applications of metal-organic frameworks**.** *Science* **2013**, *341*,1230444.

(4) Eddaoudi, M.; Sava, D. F.; Eubank, J. F.; Adil, K.; Guillerm, V. Zeolite-like metal–organic frameworks (ZMOFs): design, synthesis, and properties. *Chem. Soc. Rev*. **2015**, *44*, 228-249.

(5) Wang, L.; Han, Y.Z.; Feng, X.; Zhou, J.W.; Qi, P.F.; Wang, B. Metal–organic frameworks for energy storage: Batteries and supercapacitors. *Coordin.Chem. Rev*. **2016**, *307*, 361-381.

(6) Bétard, A.; Fischer, R. A. Metal–Organic Framework Thin Films: From Fundamentals to Applications. *Chem. Rev*. **2012**, *112*, 1055-1083.

(7) Liu, B.; Shioyama, H.; Akita, T.; Xu, Q. Metal-Organic Framework as a Template for Porous Carbon Synthesis. *J. Am. Chem. Soc*. **2008**, *130*, 5390-5391.

(8) Sun, J. K.; Xu, Q. Functional materials derived from open framework templates/precursors: synthesis and applications. *Energy. Environ. Sci*. **2014**,*7*, 2071-2100.

(9) Hao, J.H.; Yang, W.S.; Zhang, Z.; Tang, J.L.Metal-organic frameworks derived $Co_xFe_{1-x}P$ nanocubes for electrochemical hydrogen evolution. *Nanoscale* **2015**, *7*, 11055-11062.

(10) Xia, W.; Mahmood, A.; Zou, R.Q.; Xu.Q. Metal–organic frameworks and their derived nanostructures for electrochemical energy storage and conversion. *Energy. Environ. Sci*. **2015**, *8*, 1837-1866.

(11) Zhang, C.; Xiao, J.; Lv, X.L.; Qian, L.H.; Yuan, S.L.; Wang, S.P.; Lei, X. Hierarchically porous Co_3O_4/C nanowire arrays derived from a metal–organic framework for high performance supercapacitors and the oxygen evolution reaction. *J. Mater. Chem. A* **2016**, *4*, 16516-16523.

(12) Zheng, F.C.; Xia, G. L.; Yang, Y.; Chen, Q.W. MOF-derived untrafine MnO nanocrystals embedded in porous carbon matrix as high-performance anodes for lithium-ion batteries. *Nanoscale* **2015**, *7*, 9637-4965.

(13) Fe´rey, G. Hybrid porous solids: past, present, future. *Chem. Soc. Rev*. **2008**, *37*, 191-214.

(14) Hamon, L.; Serre, C.; Devic, T.; Loiseau, T.; Millange, F.; Férey, G.; De Weireld, G. Comparative study of hydrogen sulfide adsorption in the MIL-53(Al, Cr, Fe), MIL-47(V), MIL-100(Cr), and MIL-101(Cr) metal-organic frameworks at room temperature. *J. Am. Chem. Soc*. **2009**, *131*, 8775-8777.

(15) Liu, J.; Zhang, F.; Zou, X.Q.; Yu, G.L.; Zhao, N.; Fan, S.J.; Zhu, G.S. Environmentally friendly synthesis of highly hydrophobic and stable MIL-53 MOF nanomaterials. *Chem. Commun*. **2013**, *49*, 7430-7432.

(16) Zhang, C.H.; Ai, L.H. ; Jiang, J. J. Jiang, Solvothermal synthesis of MIL–53(Fe) hybrid magnetic composites for photoelectrochemical water oxidation and organic pollutant photodegradation under visible light**.** *J. Mater. Chem. A* **2015**, *3*, 3074-3081.

(17) Lu,T.; Zhang, L.C.; Sun, M.X.; Deng, D.Y.; Su, Y.Y.; Lv, Y. Amino-functionalized metal-organic frameworks nanoplates-based energy transfer probe for highly selective fluorescence detection of free chlorine. *Anal. Chem*. **2016**, *88*, 3413-3420.

(18) Hong,S.A.; Kwon,J.; Kim, D.; Yang.S. A rapid, sensitive and selective electrochemical biosensor with concanavalin A for the preemptive detection of norovirus. *Biosens. Bioelectron*. **2015**, *64*, 338-344.

(19) Priyanki, D.; Madhuri, Das.; Somasekhar, R. C.; Manoj, S. I.; Pranab, G. Recent advances on developing 3rd generation enzyme electrode for biosensor applications. *Biosens. Bioelectron*. **2016**, *79*, 386-397.

(20) Xiao, T.F.; Wu, F.; Hao, J.; Zhang, M.N.; Yu, P.; Mao, L.Q. In vivo analysis with

electrochemical sensors and biosensors. *Anal. Chem*. **2017**, *89*, 300-313.

(21) Kurbanoglu,S.; Ozkan,S.A.; Merkoci,A. Nanomaterials-based enzyme electrochemical biosensors operating through inhibition for biosensing application. *Biosens. Bioelectron*. **2017**, *89*, 886-898.

(22) Wang, Z.Y.; Dai, Z.H. Carbon nanomaterial-based electrochemical biosensors: an overview. *Nanoscale* **2015**,*7*, 6420-6431.

(23) Wang, X.; Lu, X.; Wu, L.; Chen, J. P. 3D metal-organic framework as highly efficient biosensing platform for ultrasensitive and rapid detection of bisphenol A.*Biosens. Bioelectron.* **2014**, *65C*, 295-301.

(24) Liu, T.Z.; Hu, R.; Zhang, X.; Zhang, K.L.; Liu, Y.; Zhang, X.B.; Bai, D.L.; Li, R.Y.; Yang, Y.H. Metal–organic framework nanomaterials as novel signal probes for electron transfer mediated ultrasensitive electrochemical immunoassay. *Anal. Chem*. **2016**, *88* 24, 12516-12523.

(25) Xie, S.; Ye, J.; Yuan, Y.; Chai, Y.; Yuan, R. A multifunctional hemin@metal-organic framework and its application to construct an electrochemical aptasensor for thrombin detection. *Nanoscale* **2015**, *7*, 18232-18238.

(26) Han, Y.J.; Zhai, J.F.; Zhang , L.L.; Dong, S. J. Direct carbonization of cobalt-doped NH_2-MIL-53(Fe) for electrocatalysis of oxygen evolution reaction. *Nanoscale* **2016**, *8*, 1033-1039.

(27) Peng, L.; Dong, S.Y.; Li, N.; Suo, G.C.; Huang, T.L. Construction of a biocompatible system of hemoglobin based on AuNPs-carbon aerogel and ionic

liquid for amperometric biosensor. *Sens. Actua. B*: *Chem*. **2015**, *210*, 418-424.

(28) Katz, M. J.; Brown, Z. J.; Colo´n, Y. J.; Siu, P. W.; Scheidt, K. A.; Snurr, R. Q.; Hupp, J. T.; Farha, O. K. A facile synthesis of UiO-66, UiO-67 and their derivatives.*Chem. Commun*. **2013**, *49*, 9449-9451.

(29) Chen, W.; Zhang, Z.A.; Bao, W.Z.; Lai, Y.Q.; Li, J.; Gan, Y.Q.; Wang, J.J. Hierarchical mesoporous γ-Fe_2O_3/carbon nanocomposites derived from metal organic frameworks as a cathode electrocatalyst for rechargeable Li-O_2 batteries. *Electrochim. Acta* **2014**, *134*, 293-301.

(30) Li, J. S.; Li, S.L.; Tang, Y.J.; Han, M.; Dai, Z.H.; Bao, J.C.; Lan, Y.Q. Nitrogen-doped Fe/Fe_3C@graphitic layer/carbon nanotube hybrids derived from MOFs: efficient bifunctional electrocatalysts for ORR and OER. *Chem Commun*. **2015**, *51*, 2710-2713.

(31) Bard, A. J.; Faulkner, L. R. Electrochemical Methods: Fundamentals Application. Second ed. *Wiley*, New York **1980**.

(32) G. L. Ellman, K. D. Courtney, J.V. Andres, R. M. Featherstone, A new and rapid colorimetric determination of acetylcholinesterase activity. *Biochem. Pharmacol.*, ***1961,*** *7(2)*: 88-95.

(33) Wei, M.; Wang, J. A novel acetylcholinesterase biosensor based on ionic liquidsAuNPs-porous carbon composite matrix for detection of organophosphate pesticides. *Sens. Actua. B: Chem*. **2015**, *211*, 290-296.

(34) Laviron, E. J. General expression of the linear potential sweep voltammogram in the case of diffusionless electrochemical systems. *Electroanal. Chem*. **1979**,*101*,

19-28.

(35) Kamin, R. A.; Wilson, G. S. Rotating ring-disk enzyme electrode for biocatalysis kinetic studies and characterization of the immobilized enzyme layer. *Anal. Chem*. **1980**, *52*, 1198-1205.

(36) Kandimalla, V.B.; Ju, H. Binding of acetylcholinesterase to multiwall carbon nanotube-cross-linked chitosan composite for flow-injection amperometric detection of an organophosphorous insecticide. *Chem. Eur. J*. **2006**, *12*, 1074-1080.

(37) Yu,G. X.; Wu,W. X. ; Zhao, Q.; Wei, X.Y.; Lu, Q. Efficient immobilization of acetylcholinesterase onto amino functionalized carbon nanotubes for the fabrication of high sensitive organophosphorus pesticides biosensors. *Biosens. Bioelectron*. **2015**, *68*, 288-294.

(38) Cui, H.F.; Wu, W.W.; Li, M.M.; Song, X.J.; Lv, Y.X.; Zhang, T.T. A highly stable acetylcholinesterase biosensor based on chitosan-TiO_2-graphene nanocomposites for detection of organophosphate pesticides. *Biosens. Bioelectron*. **2018**, *99*, 223-229.

(39) He, L.H. ; Cui, B.B. ; Liu, J.M. ; Song, Y.P. ; Wang, M.H. ; Peng, D.L.; Zhang, Z.H. Novel electrochemical biosensor based on core-shell nanostructured composite of hollow carbon spheres and polyaniline for sensitively detecting malathion. *Sens. Actua. B: Chem*. **2018**, *253*, 813-821.

(40) Bao, J.; Hou, C.J.; Chen, M.; Li, J.J.; Huo, D.Q.; Yang, M.; Luo, X.G.; Lei,Y. Plant esterase-chitosan/gold nanoparticles graphene nanosheet composite based

biosensor for the ultrasensitive detection of organophosphate pesticides. *J. Agric. Food Chem.* **2015**, *63*, 10319-10326.

(41) Raghu, P.; Swamy, BEK.; Reddy, TM.; Chandrashekar, BN.; Reddaiah, K. Sol–gel immobilized biosensor for the detection of organophosphorous pesticides: a voltammetric method. *Bioelectrochemistry* **2012**, *83*,19-24.

(42) Neetu, J.; Sundara, R. Development of Au nanoparticles dispersed carbon nanotube-based biosensor for the detection of paraoxon. *Nanoscale* **2010**, *2*, 806-810.

(43) Peng, L.; Dong , S.Y.; Wei, W.B.; Yuan, X.J.; Huang, T.L. Synthesis of reticulated hollow spheres structure $NiCo_2S_4$ and its application in organophosphate pesticides biosensor. *Biosens. Bioelectron*. **2017**, *94*, 563-569.

For TOC Only